New method to characterize single-cavity rf pulse compressors based on reflection measurements

Pablo Martinez-Reviriego,* Paz Alonso-Arias, Alexej Grudiev, and Ping Wang
CERN, Espl. des Particules 1, Geneva, 1217, Switzerland

(Received 19 March 2026; accepted 9 July 2026; published 7 August 2026)

Pulsed high-power radio frequency (rf) systems frequently employ pulse compressors to augment peak output power, thereby reducing the required number of rf sources and enhancing cost efficiency. A prominent class of these devices utilizes single resonant cavities supporting two degenerate modes to achieve high performance within a compact footprint. However, the inherent coupling of these modes complicates experimental characterization, a challenge exacerbated by the fact that these units are typically nondismountable. This paper proposes a novel analytical method to disentangle the complex electromagnetic data encoded within these systems. By separately extracting the parameters of the individual degenerate modes and the characteristics of the associated waveguide network, the method provides a granular view of device performance. This approach enables a more comprehensive interpretation of measurement data, offering a pathway for the precise tuning and optimization of monolithic rf pulse compression systems.

DOI: 10.1103/tzdk-c7mr

I. INTRODUCTION

High-power GHz-range radio-frequency (rf) normal-conducting devices typically operate with short rf pulses (on the order of ~100 ns) and extremely high peak powers (up to ~100 MW). To reduce the number and cost of the rf power sources (i.e., klystrons), pulse compression techniques are employed. For this purpose, high-Q resonant cavities can be used to store energy and subsequently release it in a shorter time interval, thereby increasing the output peak power.

In this configuration, energy is stored in the cavities during most of the klystron pulse and subsequently released with a controlled rf phase reversal. The pulse shape will be determined by a decay time following [1]

$$\tau = \frac{Q_0}{\pi f_0 (1+\beta)}, \tag{1}$$

where Q_0 is the unloaded quality factor, f_0 is the resonant frequency, $\beta = Q_0/Q_{\text{ext}}$ is the coupling factor, and Q_{ext} is the external quality factor of the cavity.

In addition, the peak output signal amplitude gain is given by [1]

$$\alpha = \frac{E_{\max}}{E_{\text{in}}} = \frac{2\beta}{\beta+1} + 1. \tag{2}$$

Thus, a strongly overcoupled cavity ($\beta > 1$) is required to achieve higher power gain, which is the square of the amplitude gain. In addition, a high Q_0 will increase the decay time, producing a flatter pulse. A graphical representation of this behavior is shown in Fig. 1.

Then, different approaches can be adopted to ensure that the compressed rf signal is properly directed toward the accelerating structure. Among the most established solutions is the SLAC Energy Doubler (SLED), which

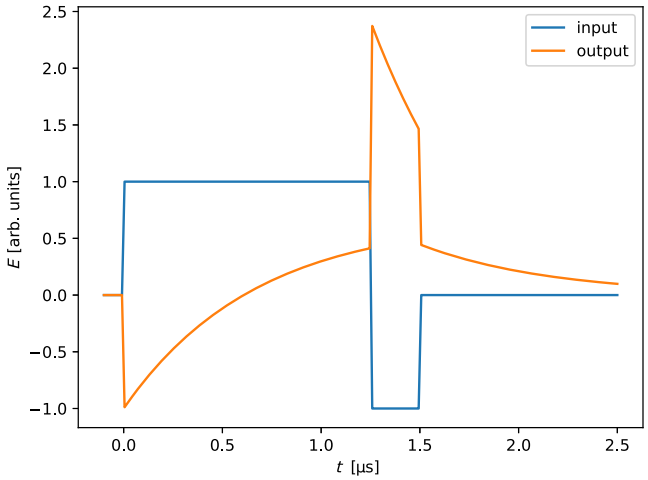


FIG. 1. Input and output amplitude signals for a resonant cavity with $Q_0 = 1.5 \times 10^5$, $Q_{\text{ext}} = 3 \times 10^4$, and $f_0 = 11.994$ GHz.

*Contact author: pablo.martinez.reviriego@cern.ch

Published by the American Physical Society under the terms of the Creative Commons Attribution 4.0 International license. Further distribution of this work must maintain attribution to the author(s) and the published article's title, journal citation, and DOI.

employs two identical high-Q resonant cavities connected through a $90° - 3$ dB hybrid [1]. An alternative approach relies on a degenerate single resonant cavity, which supports two orthogonal modes and is coupled to a circular waveguide polarizer to achieve the required directional behavior. This concept has been implemented, for instance, in bowl-shaped or spherical cavities, offering a more compact geometry and reducing the number of elements [2]. Another solution is represented by the barrel open cavity (BOC), where a single high-Q cavity is surrounded by a waveguide and coupled through multiple apertures distributed along its perimeter, allowing efficient energy extraction and pulse compression [3].

Pulse compressors are essential for the cost efficiency of normal-conducting linear accelerators, such as injectors, e^+/e^- linear colliders, or free electron lasers (FELs). Even though most devices were developed for linear colliders, including the SLED for SLAC Linear Collider, the BOC for the Very Large Electron-Positron Pilot Collider, a cavity chain based on SLED for the Japan Linear Collider, or the SLED-II for the Next Linear Collider [4–7], pulse compressors are being studied and used in other facilities such as SwissFEL, the Very Compact Inverse-Compton-Scattering Gamma-ray Source, the electron injector of the Advanced Wakefield Experiment, the Deep Electron FLASH Therapy, Xbox test facility or the Future Circular Collider injector [8–13].

II. MOTIVATION

Due to the increasing complexity of the degenerate pulse compressor cavities, the systems cannot be disentangled to provide independent measurements of each element, thereby preventing diagnosis of the fabricated prototypes. Therefore, a new analytical framework is required to explain the discrepancies observed between simulations and measurements and to enable characterization of these devices.

In particular, a klystron-based approach for the Compact Linear Collider (CLIC) at 380 GeV was studied. This strategy eliminates the need for the construction of the drive-beam complex and makes the main linac more modular [14]. In this version, two 50 MW X-band klystrons are combined to feed 8 CLIC-K accelerating structures, providing the nominal average loaded accelerating gradient of 75 MV/m [15]. To reach this gradient, each structure needs to be fed with an input power of 40.6 MW with pulses of 334 ns. This results in a total input power of ∼330 MW without taking into account rf losses. Thus, a pulse compression system made of a chain of four correction cavities and a single storage cavity was studied and designed [16,17].

Three different cavities were designed, fabricated, and tested at CERN as the prototypes for the pulse compression system of the klystron-based CLIC main linac [18]. A BOC-type was conceived for the storage cavity while two alternative approaches, based on spherical and bowl geometries, were investigated for the correction chain. Following fabrication, low-power measurement campaigns were carried out to study the rf performance and verify the design. A graphical representation of the internal (vacuum) geometries illustrating the rf design of the three cavity prototypes can be seen in Fig. 2.

In the case of the BOC prototype, an initial set of rf measurements was performed shortly after fabrication in October 2023. At this stage, the cavity was equipped with stainless steel flanges and operated under ambient conditions, without vacuum pumping or water cooling. These preliminary tests yielded satisfactory performance, confirming the expected resonant behavior. Subsequently, prior to installation in the high-power test stand, the cavity was sealed using a copper gasket with an integrated

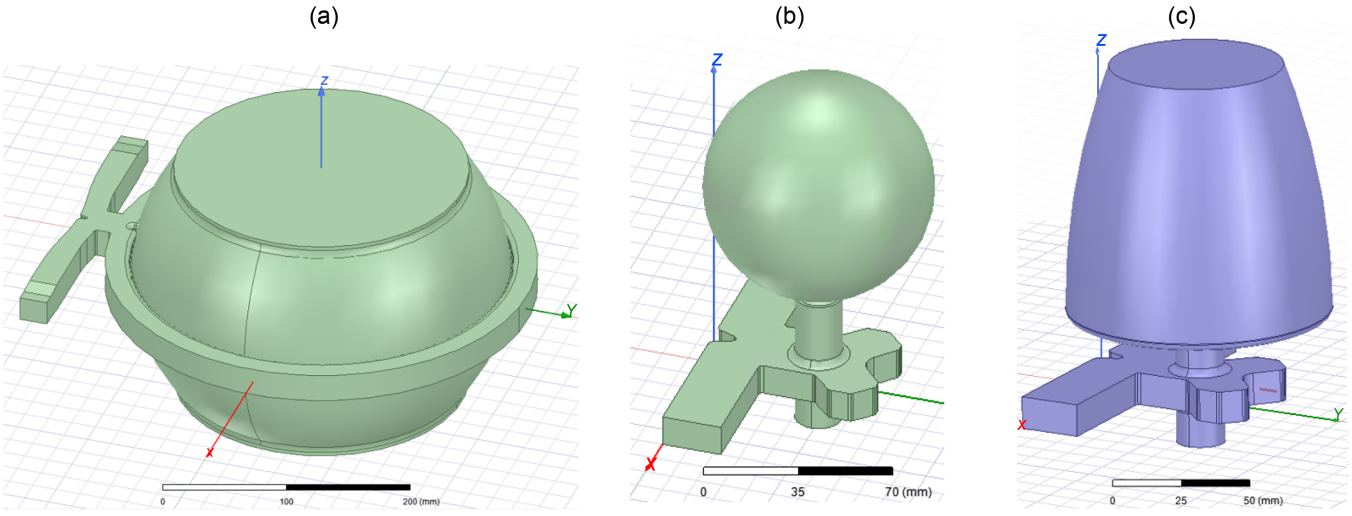


FIG. 2. Graphical representation of the vacuum geometry in the BOC (a), spherical (b), and bowl (c) prototypes for klystron-based CLIC.

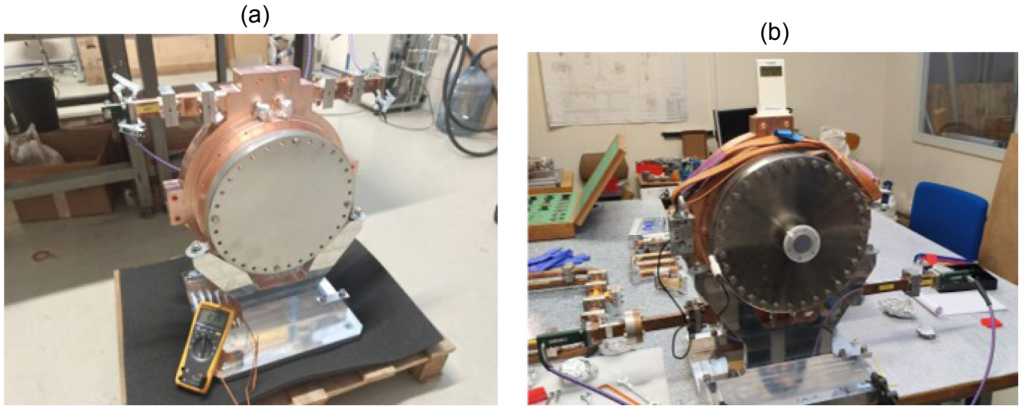


FIG. 3. BOC prototype measurement setups after fabrication (a) and before installation (b).

TABLE I. BOC prototype rf measurements comparison for different configurations.

Parameters	Design	After fabrication	Before installation
f_0 (GHz)	11.994	11.9933	11.9943
Q_0	236,000	220,194	164,200
Q_{ext}	35,800	43,883	44,480
Flanges	open	Clamped	Sealed
Vacuum	Yes	No	No
Temperature (°C)	30	23	19

pumping port, evacuated, and operated with active water cooling. Under these conditions, the measured performance was unexpectedly degraded compared to the initial results. To isolate the origin of this discrepancy, an additional measurement campaign was carried out with the cavity in the sealed configuration but without vacuum pumping or water cooling. Despite reverting to these conditions, the cavity performance remained inferior to that observed in the initial measurements. The images of both measurement setups are shown in Fig. 3. A comparison of the different configurations and their corresponding results is reported in Table I. The results are analyzed and discussed in Sec. V. It should be noted that the deviation of the measured resonant frequency from the design value is attributable to temperature differences, which induce a frequency shift of approximately $\Delta f_0[\text{MHz}] \approx 0.2\Delta T[°\text{C}]$.

Similarly, a remarkable change in the reflection parameter was found when comparing the measurements of the bowl cavity prototype before and after the final brazing step was performed. These results can be seen in Fig. 4. A picture showing the bowl prototype measurement setup is shown in Fig. 5.

The fact that these systems consist of a single cavity supporting two degenerate modes makes it difficult, or even impossible, to extract information about the individual components and modes using standard techniques, in which the two identical cavities can be detached from the hybrid and measured separately to characterize the device and find the source of the deviations from the expected value. This paper proposes a new method to decode the information provided by the measurements of the entire system, i.e., the differences in Q_0, Q_{ext}, and f_0 for the two

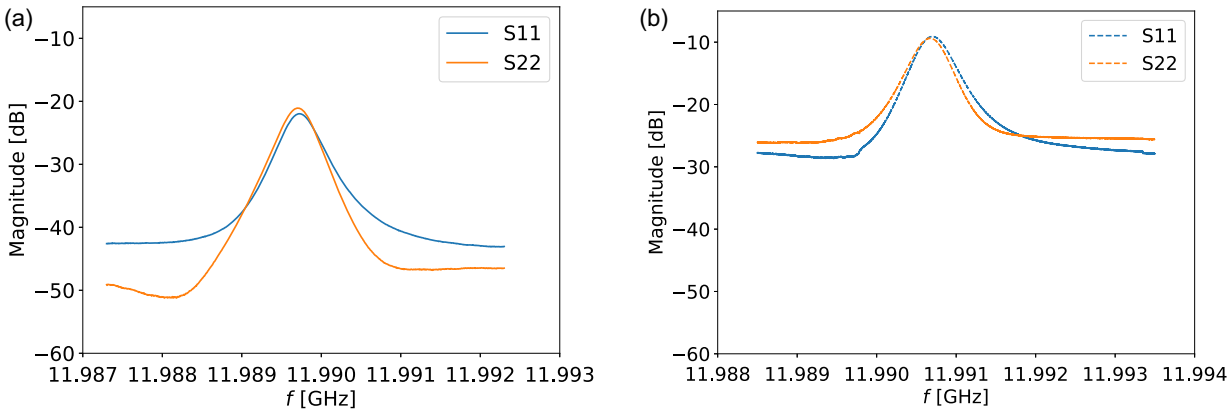


FIG. 4. Bowl cavity prototype reflection measurements before (a) and after brazing (b).

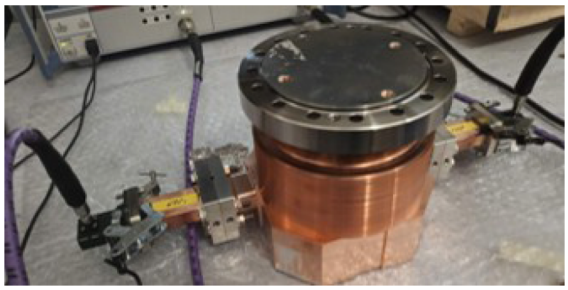


FIG. 5. Bowl cavity prototype measurement setup.

modes, as well as the S-parameters of the waveguide network, allowing for a full diagnosis.

Section III presents the foundational mathematical model underlying this study. Section IV then details the methodology employed to derive an appropriate characterization framework. In Sec. V, the results obtained to validate the proposed method are discussed. Finally, Sec. VI provides the conclusions drawn from this study.

III. MATHEMATICAL MODEL

A schematic representation of a general pulse compressor system can be seen in Fig. 6.

A mathematical model describing the dependence of the full system on the parameters of each element (including the cavities/modes and the waveguide system) will be developed to extract information from the set of measurements of the entire system.

The reflection coefficient of a resonant cavity is given by [16],

$$\Gamma = \frac{(1/Q_{\text{ext}} - 1/Q_0) - i\xi}{(1/Q_{\text{ext}} + 1/Q_0) + i\xi}, \tag{3}$$

where $i = \sqrt{-1}$ and $\xi = f/f_0 - f_0/f$ with f being the frequency.

In all cases, the full system can be characterized by a 2×2 matrix,

$$M_{\text{PC}} = \begin{pmatrix} s_{11}^{\text{PC}} & s_{21}^{\text{PC}} \\ s_{21}^{\text{PC}} & s_{22}^{\text{PC}} \end{pmatrix}, \tag{4}$$

which depends on two reflection coefficients, one for each cavity/mode, following Eq. (3), and a 4×4 matrix that

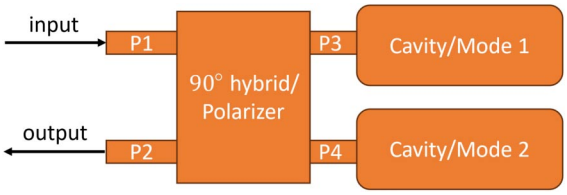


FIG. 6. Schematic view of a general pulse compressor system.

models the waveguide network. In an ideal case, the waveguide matrix takes the following form,

$$M_{\text{wg}} = \frac{1}{\sqrt{2}} \begin{pmatrix} 0 & 0 & 1 & i \\ 0 & 0 & i & 1 \\ 1 & i & 0 & 0 \\ i & 1 & 0 & 0 \end{pmatrix}, \tag{5}$$

leading to a pulse compressor matrix defined by [19,20],

$$M_{\text{PC}} = \frac{1}{2} \begin{pmatrix} \Gamma_1 - \Gamma_2 & i(\Gamma_1 + \Gamma_2) \\ i(\Gamma_1 + \Gamma_2) & \Gamma_2 - \Gamma_1 \end{pmatrix}. \tag{6}$$

For this case, an analytical calculation showing the difference needed between two cavities for each of the three parameters in order to get a maximum reflection of -30, -20, and -10 dB can be seen in Fig. 7.

It can be observed that unmatched f_0 and Q_0 result in a single peak reflection while the Q_{ext} leads to a double peak. In all cases, the reflection decays as we move away from the resonant frequency.

However, this model exhibits several limitations, as it cannot capture nonsymmetric behaviors such as $|s_{11}^{\text{PC}}| \neq |s_{22}^{\text{PC}}|$, nonzero asymptotic reflections, or imperfections arising from the waveguide network itself. Therefore, the main contribution of this work lies in the introduction of a more realistic framework. In this context, the waveguide matrix can be generalized using the following form,

$$M_{\text{wg}} = \begin{pmatrix} s_{11} & s_{21} & s_{31} & s_{41} \\ s_{21} & s_{22} & s_{41} & s_{31} \\ s_{31} & s_{41} & s_{33} & s_{43} \\ s_{41} & s_{31} & s_{43} & s_{44} \end{pmatrix}, \tag{7}$$

where we assumed $s_{32} = s_{41}$ and $s_{42} = s_{31}$, leading to a pulse compressor system defined as [19],

$$s_{11}^{\text{PC}} = s_{11} + \frac{s_{41}^2(1/\Gamma_1 - s_{33}) + s_{31}^2(1/\Gamma_2 - s_{44}) + 2s_{41}s_{31}s_{43}}{(1/\Gamma_2 - s_{44})(1/\Gamma_1 - s_{33}) - s_{43}^2}, \tag{8}$$

$$s_{22}^{\text{PC}} = s_{22} + \frac{s_{31}^2(1/\Gamma_1 - s_{33}) + s_{41}^2(1/\Gamma_2 - s_{44}) + 2s_{41}s_{31}s_{43}}{(1/\Gamma_2 - s_{44})(1/\Gamma_1 - s_{33}) - s_{43}^2}. \tag{9}$$

Some examples of reflections from a system characterized by a 10 kHz difference between the two cavities and a mismatched waveguide are shown in Fig. 8.

In this case, it can be observed that the system is no longer symmetric and the reflection shows an asymptotic behavior when we move away from the resonant frequency. In practice, a combination of all the above imperfections results in measured reflections from a cavity, as shown, for example, in Fig. 4.

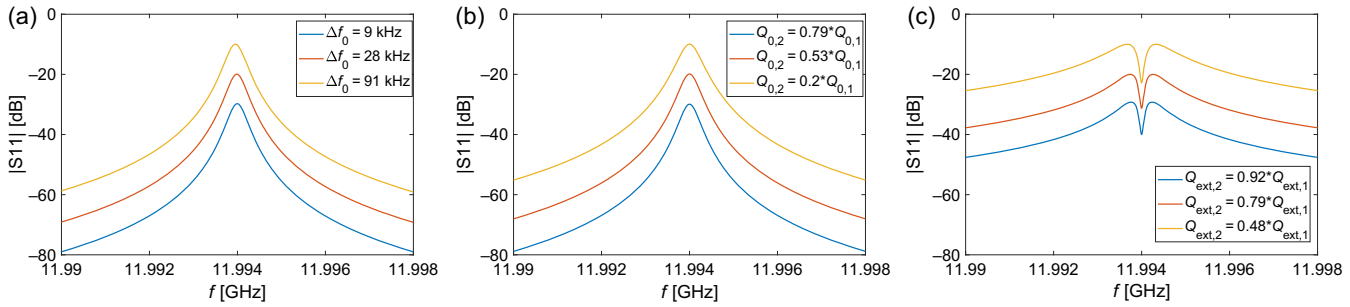


FIG. 7. Analytical calculation of the difference required in f_0 (a), Q_0 (b), and Q_{ext} (c) for a pulse compressor with ideal waveguide network to get a maximum reflection of −30 (blue), −20 (red), and −10 (yellow) dB. Design parameters: $f_{0,1} = 11.994$ GHz, $Q_{0,1} = 1.7 \times 10^5$, and $Q_{\text{ext},1} = 3 \times 10^4$.

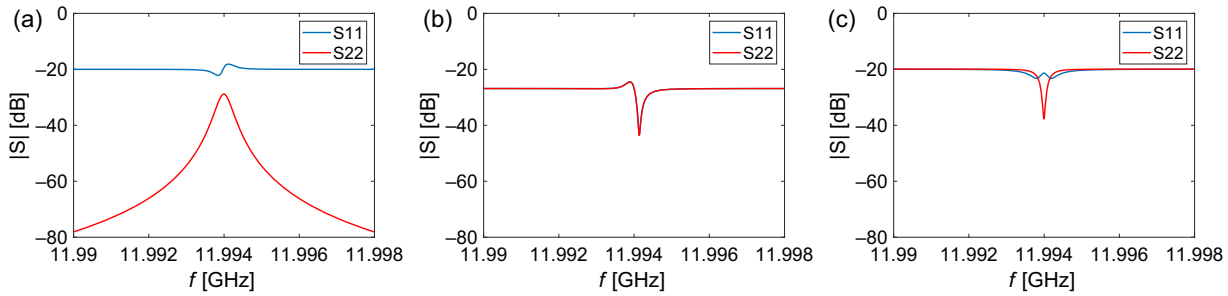


FIG. 8. Analytical calculation for a system characterized by $\Delta f_0 = 10$ kHz and $s_{11} = 0.1$ (a), $s_{33} = 0.1$ (b), and $s_{43} = 0.1$ (c). In (b), both curves overlap. Design parameters: $f_{0,1} = 11.994$ GHz, $Q_{0,1} = 1.7 \times 10^5$, and $Q_{\text{ext},1} = 3 \times 10^4$.

IV. METHODOLOGY

First, the measurement of s_{21}^{PC} is used to obtain estimates of the average values of Q_0, Q_{ext}, and f_0 over the two modes by fitting the data to a mathematical expression of the form

$$s_{21}^{\text{PC}} = \frac{(1/Q_{\text{ext}} - 1/Q_0) - i\xi}{(1/Q_{\text{ext}} + 1/Q_0) + i\xi} e^{i\delta} + af + b, \tag{10}$$

where δ, a, and b account for the phase shift and attenuation that could not be considered in the calibration. In addition, a weighting factor, $w = 1 - |s_{21}^{\text{PC}}|^2$, corrects for the deviation from a perfect circle with increasing distance from f_0 and for the lower density of measurement points around the critical frequency, following the reasoning presented in [21]. An example of the fit is shown in Fig. 9 for the BOC prototype measurement before installation presented in Sec. II, and the values obtained can be found in Table II.

In a second step, using the fitted values of f_0, Q_0, and Q_{ext} as initial guesses, the measurements of s_{11}^{PC} and s_{22}^{PC} are fitted to Eqs. (8) and (9), respectively, using the same weighting factor as in the first step. The fitting algorithm

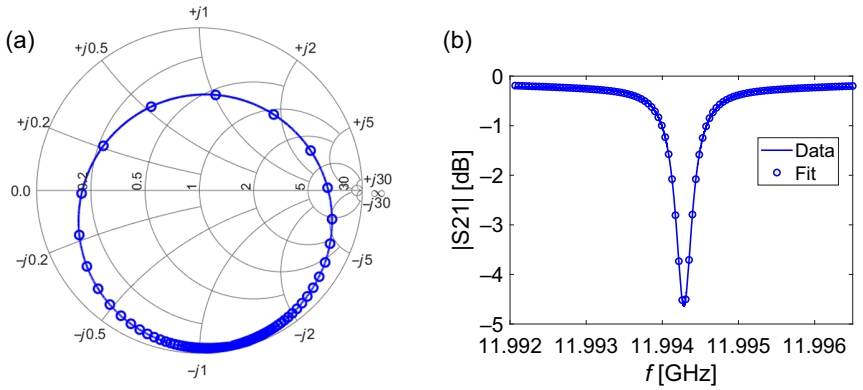


FIG. 9. s_{21}^{PC} measurement and fit in Smith chart (a) and dB (b) for the BOC prototype before installation.

TABLE II. Cavity parameters from s_{21}^{PC} fit.

Fit parameters	Value
f_0 (GHz)	11.9943
Q_0	164,265
Q_{ext}	44,535

used was the *lsqnonlin* from MATLAB [22] after applying the following settings:

1. Initial guess was obtained from s_{21}^{PC} fit and from ideal waveguide in Eq. (5).
2. Fit is centered at f_0.
3. Phase difference locked in the hybrid: $s_{31} = |s_{31}|e^{i\phi}$ and $s_{41} = |s_{41}|e^{i(\phi+\pi/2)}$.
4. Bounds: lower and upper bounds were set for all parameters.
   (i) $|\Re(s_{ii})|, |\Im(s_{ii})|, |\Re(s_{43})|, |\Im(s_{43})| < 0.3$.
   (ii) $1/\sqrt{2} - 0.3 < |s_{31}|, |s_{41}| \leq 1/\sqrt{2}$.
   (iii) $0.5Q_{ext} < Q_{ext,i} < 1.5Q_{ext}$.
   (iv) $0.5Q_0 < Q_{0,i} \leq Q_0$.
   (v) $|\Delta f_0| < 2$ [MHz].

A graphical representation of the solution obtained for the s_{11}^{PC} and s_{22}^{PC} measurement of the BOC prototype can be seen in Fig. 10.

This two-step fitting allows us to find the values for the two modes, as well as the S-parameters of the nonideal waveguide network, as shown in Table III, where Δf_0, ΔQ_0, and ΔQ_{ext} correspond to the differences between the two modes in resonant frequency, unloaded quality factor, and external quality factor, respectively, and $|s_{ij}|$ is the absolute value of the corresponding element of the waveguide network matrix.

Due to the nonlinear nature of the fitting problem and the relatively large number of free parameters involved, the existence of multiple local minima cannot be excluded *a priori*. In practice, the fitting procedure is guided toward physically meaningful solutions through physically motivated initial conditions and parameter

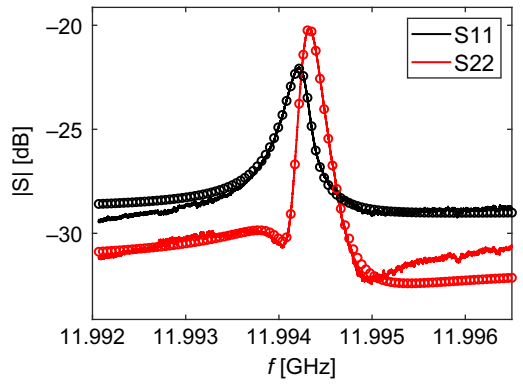


FIG. 10. s_{11}^{PC} and s_{22}^{PC} measurements (solid line) and fits (circles) in dB for a BOC prototype.

TABLE III. Full system parameters from s_{11}^{PC}, s_{22}^{PC} fit for the BOC prototype measurements.

Fit parameters	Value
Δf_0 (kHz)	14.45
ΔQ_0 (%)	10.30
ΔQ_{ext} (%)	5.06
$\|s_{11}\|$	0.029
$\|s_{22}\|$	0.038
$\|s_{33}\|$	0.050
$\|s_{44}\|$	0.042
$\|s_{43}\|$	0.013
$\|s_{31}\|$	0.688
$\|s_{41}\|$	0.707

bounds. Nevertheless, different parameters do not affect the measured response with the same sensitivity. For this reason, a dedicated sensitivity analysis was performed to evaluate the robustness and identifiability of each reconstructed parameter. For this purpose, we use the Θ function, defined as

$$\Theta = \sqrt{\frac{1}{N}\sum_j [w_j(y_j - y_j^{exp})]^2}, \tag{11}$$

where N corresponds to the number of points, and y, y^{exp} represent the mathematical and experimental complex values of s_{11}^{PC} and s_{22}^{PC}.

Parameters producing a sharp minimum of the Θ function are considered well identified, since small variations lead to a significant degradation of the agreement between model and measurement. Conversely, broad minima indicate weak sensitivity and therefore reduced confidence in the uniqueness of the reconstructed parameter. An example of the dependence of Θ with respect to Δf_0 can be seen in Fig. 11.

Δf_0^* corresponds to the optimum value of the parameter, and δ_{min} and δ_{max} represent the deviations needed to

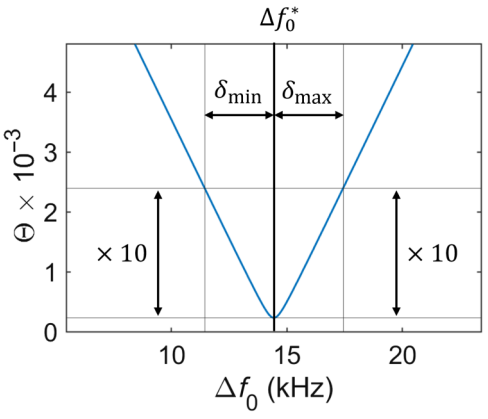


FIG. 11. Θ function dependence on the Δf_0. Error bars are estimated when Θ increases by a factor 10 compared to the minimum value.

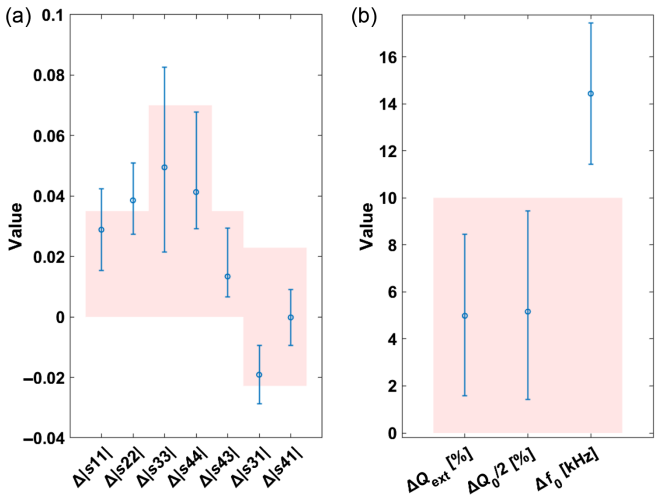


FIG. 12. Representation of final results for the waveguide network (a) and modes parameters (b) from applying the method to s_{11}^{PC} and s_{22}^{PC} BOC prototype measurements.

increase the Θ function by a factor 10 compared to the minimum value, leading to an estimation of the error bars. The final result for the parameter will be given as

$$\Delta f_0 = \Delta f_{0-\delta_{\min}}^{*+\delta_{\max}}. \tag{12}$$

The results for all parameters of this example can be seen in Fig. 12.

Here, Δs_{ij} represents the difference between the fitted waveguide network parameters and the ideal case, and Δf_0, ΔQ_0, and ΔQ_{ext} are the differences between the two cavities or modes. The red area represents the minimum parameter deviation, with all other parameters held at their ideal values, required in the numerical evaluation of Eqs. (8) and (9) to produce a maximum reflection of −30 dB, which is adopted as a threshold below which deviations from the ideal values have a negligible impact on system performance.

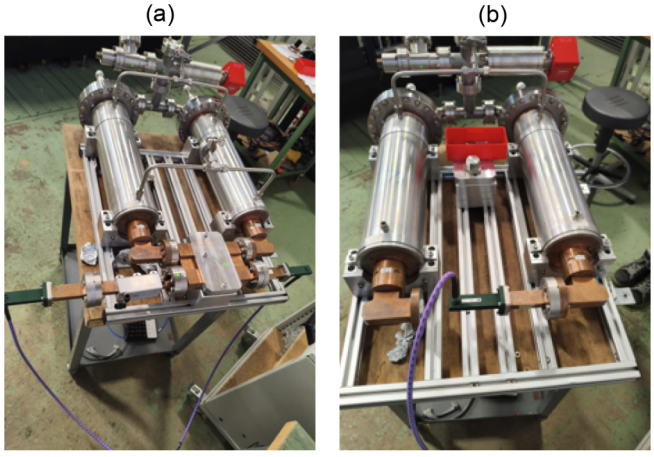


FIG. 13. Full Xbox2 SLED-type pulse compressor measurement (a) and independent cylinder cavity measurements setup (b).

V. RESULTS

The method was validated through a series of tests to demonstrate its stability and repeatability. It was verified that the difference between the results was below −30 dB after measuring the same device in the same conditions with different VNAs. In addition, it was observed that exchanging numerically the ports, i.e., $s_{11}^{\mathrm{PC}} \leftrightarrow s_{22}^{\mathrm{PC}}$, results in the exchange of all fit parameters except for the s_{31} and s_{41}. This behavior is expected from a mathematical point of view as a consequence of the assumptions $s_{32} = s_{41}$ and $s_{42} = s_{31}$. In addition, variations of the initial guess and fitting bounds were tested numerically and did not produce significant changes in the reconstructed parameters within the estimated sensitivity intervals, as shown in the Appendix. Finally, there was no significant dependence after changing the number of points in the fit or the bounds referenced in the previous section. First, the method is verified using a SLED-type pulse compressor used in Xbox2. Subsequently, it is applied to analyze the three prototypes designed and fabricated for the klystron-based CLIC rf pulse compression system. The fitting results for s_{11}^{PC} and s_{22}^{PC} are then compared with the values obtained from simulations of the ideal geometry performed using the CST studio suite [23] Frequency Domain Solver, as well as with all measurements carried out on the cavities.

A. Xbox2 SLED-type pulse compressor

The pulse compressor used in the X-band test stand Xbox2 [24] at CERN was first measured as a full system, followed by measurements of the separated components: two cavities (bottles) and −3 dB-hybrid coupler for comparison as a benchmark of the method. A picture of the measurement setup is shown in Fig. 13. The results for the s_{21}^{PC} measurements can be seen in Table IV.

Then, a comparison between the individual measurements of the hybrid and the two cavities and the values obtained using the full system measurements of s_{11}^{PC} and s_{22}^{PC} is shown in Fig. 14. It can be seen that, while there is a small overestimation of the Δf_0, the agreement is good, demonstrating the validity of the new method.

B. BOC prototype for klystron-based CLIC

For the BOC prototype, shown in Fig. 3, the average values obtained from the s_{21}^{PC} measurements are shown in Table I. The results from the fit can be seen in Fig. 15.

TABLE IV. Xbox2 SLED-type rf measurements of the full system.

Parameters	Design	SLED fit	Cavity 1	Cavity 2
f_0 (GHz)	11.994	11.9916	11.99142	11.99142
Q_0	1.8×10^5	157,728	164,532	158,762
Q_{ext}	3×10^4	29,654	31,225	30,906

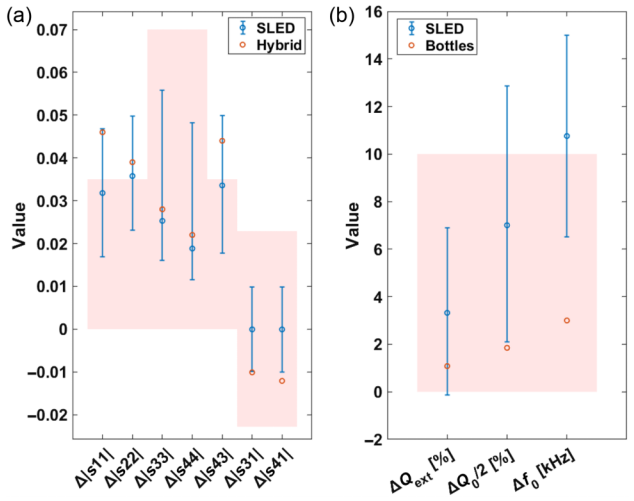


FIG. 14. Comparison between the direct measurement of the full pulse compressor system and the results obtained from the method for the waveguide network (a) and both cavities (b).

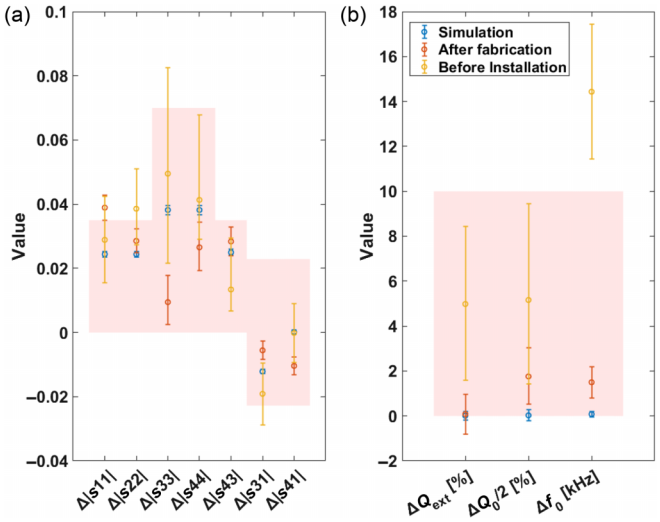


FIG. 15. Comparison of BOC prototype results for the waveguide network (a) and modes parameters (b).

The largest deviation within the region of non-negligible reflection corresponds to an increased frequency difference between the measurement taken after fabrication and the one taken before installation. This frequency shift is likely caused by a deformation of the cavity volume. Although the exact mechanism is still uncertain, possible contributors include stresses introduced during the installation of the two big vacuum flanges and waveguides or external pressure applied during vacuum pumping. In contrast, the remaining parameters overlap within regions that exhibit reflection levels below −30 dB.

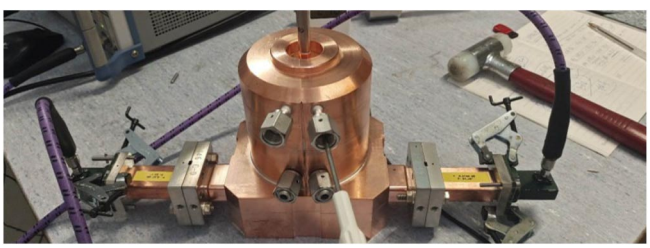


FIG. 16. Spherical cavity prototype measurement setup for klystron-based CLIC.

TABLE V. Spherical cavity prototype rf measurements of the full system.

Parameters	Design	Before brazing	After brazing	Before tuning	After tuning
f_0 (GHz)	11.994	11.991	11.9907	11.9909	11.9927
Q_0	71,000	69,927	68,234	69,063	68,827
Q_{ext}	36,400	36,677	37,085	35,550	29,997

C. Spherical cavity prototype for klystron-based CLIC

Regarding the spherical cavity prototype, several measurements were performed after fabrication: the first one before brazing, followed by three additional measurements after brazing—one before and two after the rf tuning procedure. A picture of the setup for the spherical cavity prototype is shown in Fig. 16. The results for the average measurement can be seen in Table V.

The full results are shown in Fig. 17. A consistent frequency shift and a deviation from the ideal polarizer behavior are observed in all measurements taken after brazing. This suggests that a deformation of the cavity and/or a misalignment between the polarizer and the cavity coupling hole may have occurred during the brazing process, leading to a loss of symmetry and mode degeneracy in the cavity, as well as a slightly elliptical polarization in the waveguide network.

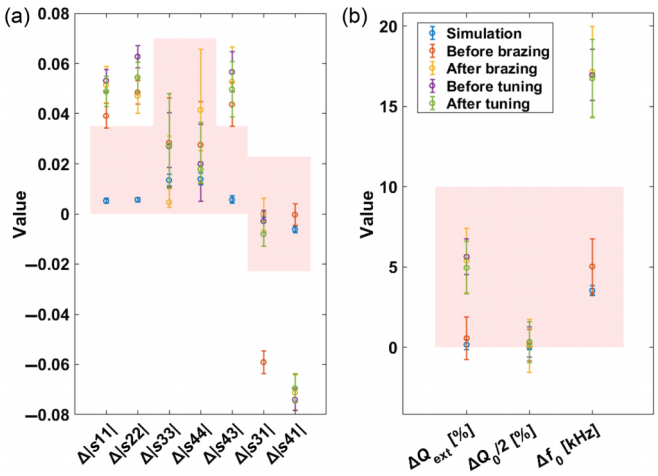


FIG. 17. Comparison of spherical cavity prototype results for the waveguide network (a) and modes parameters (b).

TABLE VI. Bowl cavity prototype rf measurements of the full system.

Parameters	Design	Before brazing	After brazing
f_0 (GHz)	11.994	11.9897	11.9907
Q_0	7.5×10^4	69,340	56,872
Q_{ext}	3.81×10^4	27,283	25,286

D. Bowl cavity prototype for klystron-based CLIC

Finally, the bowl cavity prototype shown in Fig. 5 was measured before and after brazing. The averaged results can be seen in Table VI.

Then, the full results are plotted in Fig. 18. Before brazing, the frequency split was approximately $\Delta f_0 \approx 30$ kHz, but it degraded significantly after the brazing procedure to about $\Delta f_0 \approx 120$ kHz. In addition, the performance of the waveguide network parameters is noticeably worse; however, it is not clear whether this is an actual physical effect or an artifact caused by the large separation between the two modes.

VI. CONCLUSIONS

Single-cavity pulse compressors are challenging to diagnose due to the coexistence of degenerate modes and the inability to characterize them individually. This work proposes a method to characterize and disentangle the information concealed in these complex systems by using the full set of measurements $s_{21}^{\text{PC}}, s_{11}^{\text{PC}}, s_{22}^{\text{PC}}$ instead of only s_{21}^{PC} used in the standard measurement procedure.

From a mathematical point of view, it was concluded that reflections in this kind of system arise mainly from differences in the two cavities/modes involved: ΔQ_{ext} causes a double-peak reflection, while $\Delta f_0, \Delta Q_0$ lead to a single peak. However, nonsymmetric behavior, $s_{11}^{\text{PC}} \neq s_{22}^{\text{PC}}$, or asymptotic values of reflections can only be produced by perturbations in the waveguide system coupling rf power to the two cavities/modes.

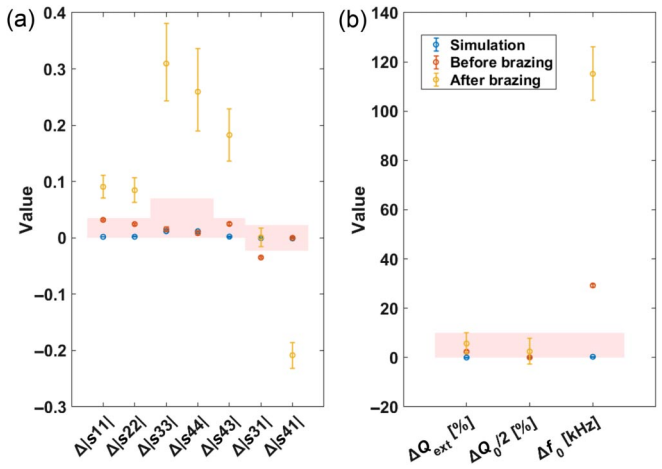


FIG. 18. Comparison of bowl cavity prototype results for the klystron-based CLIC for the waveguide network (a) and modes parameters (b).

The method was validated using the SLED-type pulse compressor from Xbox2, for which the individual components could be characterized independently, and demonstrated excellent agreement across all simulated structures. Then, it was used to study the deviation from the expected performance of the BOC prototype, attributed to a deformation or modification of the cavity volume before installation. In addition, it pointed to a possible deformation induced during the final brazing step in a spherical and, especially, in a bowl cavity. In some cases, degradation in the coupling waveguide network parameters suggests its possible deformation or misalignment during the final brazing step or postfabrication handling. In all cases, the degeneracy loss induced by the deformation seems to be responsible for the lower performance of the pulse compressors.

The results consistently show that the dominant source of performance degradation across all three prototypes is the loss of mode degeneracy (Δf_0), primarily induced by brazing or postassembly mechanical stress. This suggests that tighter dimensional tolerances and thermal management during brazing, particularly for cavities where the two degenerate modes are sensitive to volume asymmetry, would have the greatest impact on final rf performance. Similarly, the waveguide network coupling parameters (s_{31}, s_{41}) are shown to be critical, and their deviation from the ideal 90° hybrid behavior directly produces asymmetric reflection, pointing to the importance of precise alignment and interface control at the polarizer-cavity junction. In contrast, the sensitivity analysis reveals that Δs_{33} and Δs_{44} are consistently the least sensitive parameters across all cases studied, remaining within the −30 dB uncertainty region. This suggests that moderate imperfections in the self-reflection at the cavity-facing ports of the waveguide network have a negligible impact on system performance and that fabrication tolerances for these elements may therefore be relaxed relative to those governing Δf_0, s_{31}, s_{41}, and s_{43}.

ACKNOWLEDGMENTS

The authors are grateful to Nuria Catalan-Lasheras, Igor Syratchev, and Walter Wuensch for their valuable comments, and to Sergio González-Antón for assembling the measurement setup.

DATA AVAILABILITY

The data that support the findings of this article are openly available [25], embargo periods may apply.

APPENDIX: CONVERGENCE CHECK

The stability of the results for variations in the initial guesses and fitting bounds was studied and is shown in

TABLE VII. Sensitivity of the results to variations in the initial guess.

Initial guess	Original	$\Re(s_{ii}), \Im(s_{ii}) = 0.02$	$\lvert s_{31}\rvert, \lvert s_{41}\rvert = 1/\sqrt{2} - 0.02$	$Q_{\mathrm{ext},i} = 1.1Q_{\mathrm{ext}}$	$Q_{0,i} = 1.1Q_0$	$f_{0,i} = f_0 + 1$ (kHz)
$\Delta\lvert s_{11}\rvert$	$0.029^{+0.014}_{-0.013}$	0.029	0.021	0.03	0.029	0.029
$\Delta\lvert s_{22}\rvert$	$0.039^{+0.012}_{-0.011}$	0.041	0.045	0.04	0.04	0.038
$\Delta\lvert s_{33}\rvert$	$0.05^{+0.03}_{-0.03}$	0.08	0.03	0.019	0.06	0.03
$\Delta\lvert s_{44}\rvert$	$0.041^{+0.026}_{-0.012}$	0.09	0.014	0.05	0.012	0.023
$\Delta\lvert s_{43}\rvert$	$0.013^{+0.016}_{-0.007}$	0.014	0.014	0.013	0.016	0.013
$\Delta\lvert s_{31}\rvert$	$-0.019^{+0.010}_{-0.010}$	−0.018	−0.04	−0.019	−0.02	−0.02
$\Delta\lvert s_{41}\rvert$	$0.000^{+0.009}_{-0.009}$	0.0004	−0.02	−0.0003	−0.0015	−0.0004
$\Delta Q_{\mathrm{ext}}[\%]$	5^{+3}_{-3}	4	2	6	4	5
$\Delta Q_0/2[\%]$	5^{+4}_{-4}	5	6	5	4	6
Δf_0(kHz)	14^{+3}_{-3}	14	15	14	15	14

TABLE VIII. Sensitivity of the result to variations in the fitting bounds.

Fitting bounds	Original	$\Re(s_{ii}), \Im(s_{ii}) \lesssim \pm 0.5$ and $\lvert s_{31}\rvert, \lvert s_{41}\rvert \lesssim 1/\sqrt{2} \pm 0.5$	$Q_{\mathrm{ext},i} \lesssim (1 \pm 0.75)Q_{\mathrm{ext}}$	$Q_{0,i} \lesssim (1 \pm 0.75)Q_0$	$\lvert\Delta f_0\rvert < 4$ (MHz)
$\Delta\lvert s_{11}\rvert$	$0.029^{+0.014}_{-0.013}$	0.031	0.033	0.027	0.029
$\Delta\lvert s_{22}\rvert$	$0.039^{+0.012}_{-0.011}$	0.038	0.036	0.039	0.039
$\Delta\lvert s_{33}\rvert$	$0.05^{+0.03}_{-0.03}$	0.05	0.03	0.03	0.04
$\Delta\lvert s_{44}\rvert$	$0.041^{+0.026}_{-0.012}$	0.08	0.07	0.026	0.037
$\Delta\lvert s_{43}\rvert$	$0.013^{+0.016}_{-0.007}$	0.013	0.013	0.013	0.013
$\Delta\lvert s_{31}\rvert$	$-0.019^{+0.010}_{-0.010}$	−0.017	−0.018	−0.019	−0.019
$\Delta\lvert s_{41}\rvert$	$0.000^{+0.009}_{-0.009}$	0.001	0.000	0.000	0.000
$\Delta Q_{\mathrm{ext}}[\%]$	5^{+3}_{-3}	6	7	4	5
$\Delta Q_0/2[\%]$	5^{+4}_{-4}	4	5	6	5
Δf_0(kHz)	14^{+3}_{-3}	14	14	14	14

Tables VII and VIII, respectively, for the BOC prototype measurement shown presented in Fig. 12.

It can be seen that modifying the initial guesses and fitting bounds produces only minor variations in the fitted parameters. Among them, s_{33} and s_{44} exhibit the largest absolute changes, which is expected given their lower sensitivity in the fitting procedure. However, these variations remain below the parameter sensitivities and within the error margins defined by the −30 dB confidence belt. Therefore, the main conclusion of the analysis, that the observed misbehavior is primarily caused by the difference in the resonant frequencies of the two modes, remains unchanged for all the cases considered.

[1] Z. Farkas, H. Hogg, G. Loew, and P. B. Wilson, SLED: A method of doubling SLAC's energy, in *Proceedings of the International Conference on High Energy Accelerators* (SLAC, 1974), p. 576.

[2] J. W. Wang, S. G. Tantawi, C. Xu, M. Franzi, P. Krejcik, G. Bowden, S. Condamoor, Y. Ding, V. Dolgashev, J. Eichner, A. Haase, J. R. Lewandowski, and L. Xiao, Development for a supercompact X-band pulse compression system and its application at SLAC, Phys. Rev. Accel. Beams **20**, 110401 (2017).

[3] I. Syrachev, The progress of X-band "open" cavity rf pulse compression systems, in *Proceeding of 4-th European Particle Accelerator Conference, London, UK* (1994), pp. 375–379.

[4] R. Akre, V. Bharadwaj, P. Emma, and P. Krejcik, SLAC linac rf performance for LCLS, arXiv:physics/0008171.

[5] V. Balakin and I. Syrachev, Status of VLEPP rf power multiplier (VPM), in *Proceedings of EPAC92* (1992), p. 1173.

[6] H. Matsumoto, S. Win, S. Takeda, Y. Takasu, and M. Yoshida, The KEK c-band rf system for a linear collider, in *LINAC'04* (2004).

[7] S. G. Tantawi, C. D. Nantista, V. A. Dolgashev, C. Pearson, J. Nelson, K. Jobe, J. Chan, K. Fant, J. Frisch, and D. Atkinson, High-power multimode X-band rf pulse compression system for future linear colliders, Phys. Rev. ST Accel. Beams **8**, 042002 (2005).

[8] T. Schietinger, M. Pedrozzi, M. Aiba, V. Arsov, S. Bettoni, B. Beutner, M. Calvi, P. Craievich, M. Dehler, F. Frei *et al.*, Commissioning experience and beam physics measurements at the swissfel injector test facility, Phys. Rev. Accel. Beams **19**, 100702 (2016).

[9] X.-C. Lin, H. Zha, J.-R. Shi, Q. Gao, J.-Y. Liu, L.-Y. Zhou, J. Gao, H.-B. Chen, and C.-X. Tang, Fabrication, tuning, and high-gradient testing of an X-band traveling-wave accelerating structure for VIGAS, Nucl. Sci. Tech. **33**, 102 (2022).

[10] E. Gschwendtner, K. Lotov, P. Muggli, M. Wing, R. Agnello, C. C. Ahdida, M. C. Amoedo Goncalves, Y. Andrebe, O. Apsimon, R. Apsimon *et al.*, The AWAKE run 2 programme and beyond, Symmetry **14**, 1680 (2022).

[11] M. E. Angoletta *et al.*, The DEFT facility: An accelerator for very-high-energy electron FLASH radiotherapy—Technical design report, Tech. Rep. (2025), Vol. **7**.

[12] N. Catalan-Lasheras, J. Kovermann, G. McMonagle, W. Farabolini, B. Woolley, S. Doebert, A. Degiovanni, I. Syratchev, S. Rey, L. Timeo *et al.*, Experience operating an X-band high-power test stand at CERN, Tech. Rep. (2014).

[13] A. Kurtulus, S. Doebert, Y. Zhao, A. Latina, and A. Grudiev, RF design and optimization of Linacs for the CLIC main beam injector complex, Tech. Rep. (2025).

[14] CLIC. T., T. Charles, P. Giansiracusa, T. Lucas, R. Rassool, M. Volpi, C. Balazs, K. Afanaciev, V. Makarenko, A. Patapenka *et al.*, The compact linear collider (CLIC)-2018 summary report, arXiv:1812.06018.

[15] J. Liu and A. Grudiev, rf design of accelerating structure for the main linac of the klystron-based first stage of CLIC at 380 GeV, Tech. Rep. (2018).

[16] P. Wang, H. Zha, I. Syratchev, J. Shi, and H. Chen, rf design of a pulse compressor with correction cavity chain for klystron-based compact linear collider, Phys. Rev. Accel. Beams **20**, 112001 (2017).

[17] P. Wang, M. Capstick, N. C. Lasheras, S. Doebert, A. Grudiev, C. Rossi, P. M. Sanchez, I. Syratchev, and X. Wu, Design of the rf waveguide network for the klystron-based clic main linac rf module, Nucl. Instrum. Methods Phys. Res. Sect. A **1064**, 169410 (2024).

[18] P. Wang, A. Grudiev, B. Riffaud, E. Berthome, F. Motschmann, I. Syratchev, K. Scibor, L. Giordanino, N. C. Lasheras, and P. M. Scanchez, Design, fabrication and rf measurements of the storage and correction cavity prototypes of the rf pulse compression system for the klystron-based CLIC main linac, Nucl. Instrum. Methods Phys. Res. Sect. A **1084**, 171192 (2026).

[19] P. Wang and A. Grudiev, Single cylinder-based rf-cavity-system types for correction cavities in a klystron-based compact linear collider, Phys. Rev. Accel. Beams **28**, 032002 (2025).

[20] X. Lin, H. Zha, J. Shi, Y. Jiang, F. Hu, W. Gu, Q. Gao, and H. Chen, X-band two-stage rf pulse compression system with correction cavity chain, Phys. Rev. Accel. Beams **25**, 120401 (2022).

[21] H. W. Pommerenke, U. van Rienen, and A. Grudiev, rf measurements and tuning of the 1-m-long 750 MHz radio-frequency quadrupole for artwork analysis, Nucl. Instrum. Methods Phys. Res. Sect. A **1011**, 165564 (2021).

[22] The MathWorks Inc., MATLAB version: 24.1.0 (R2024a), The MathWorks Inc., 2024, https://www.mathworks.com.

[23] CST particle studio, https://www.3ds.com/products/simulia/cst-studio-suite.

[24] B. Woolley, I. Syratchev, and A. Dexter, Control and performance improvements of a pulse compressor in use for testing accelerating structures at high power, Phys. Rev. Accel. Beams **20**, 101001 (2017).

[25] https://edms.cern.ch/document/2960996/2; https://edms.cern.ch/document/3162440/1; https://edms.cern.ch/document/3162442/1.